

# Measuring marine self-potential using an autonomous underwater vehicle

Steven Constable,<sup>1</sup> Peter Kowalczyk<sup>2</sup> and Steve Bloomer<sup>2</sup>

<sup>1</sup>Scripps Institution of Oceanography, University of California San Diego, La Jolla, CA 92037, USA. E-mail: [sconstable@ucsd.edu](mailto:sconstable@ucsd.edu)

<sup>2</sup>Ocean Floor Geophysics, Vancouver, BC V5J5J3, Canada

Accepted 2018 June 29. Received 2017 July 26; in original form 2018 June 20

## SUMMARY

The marine self-potential (SP) method is used to explore for hydrothermal venting and associated seafloor mineralization. Measurements are commonly made in deep water using instruments towed close to the seafloor, which requires dedicated ship time, is limited to slow speeds, and is subject to navigation errors. Instead, we mounted a three-axis electric field receiver on an autonomous underwater vehicle (AUV), and tested the method with data collected in the Iheya area of the Okinawa Trough, off Japan. Parts of this prospect have documented hydrothermal venting and seafloor massive sulfide (SMS) deposits. An International Submarine Engineering Limited explorer-class AUV was fitted with a controlled-source electromagnetic (CSEM) amplifier and logging system, modified to collect DC SP data using silver chloride electrodes on approximately 1 m dipoles. A 1 km × 1 km area was surveyed with a flight pattern of six lines, collected three times to assess repeatability and noise levels. The entire data set was collected in a single day on station with a 10 hr AUV deployment. Flying height was 70 m, navigation errors were less than 3 m, collection speed was 1.1 m s<sup>-1</sup> and electric field noise levels were less than 5 µV m<sup>-1</sup>. Localized anomalies of 0.3 mV m<sup>-1</sup> were observed, from which potentials were estimated using regularized inversion, yielding negative SP anomalies of 15–25 mV. Modelling electric field data as dipoles shows that the negative poles causing the anomalies are localized near the seafloor with a diffuse return current deeper than 1000 m below seafloor. Apparent conductivities as high as 30 S m<sup>-1</sup> were derived from CSEM data collected during the same deployment, which strongly suggests that SMS mineralization is associated with one of the SP anomalies, although the localization near the seafloor and the lack of a dipolar signal suggest that the causative mechanism for the SP anomalies is due to hydrothermal venting. In either case, we have demonstrated that AUV-mounted instrument systems are an efficient, effective and low noise means of collecting marine SP data.

**Key words:** Hydrothermal systems; Submarine tectonics and volcanism; Electromagnetic methods.

## 1 INTRODUCTION

Using electric self-potentials (SPs) as a means to study geology, and metalliferous ore bodies in particular, dates from R.W. Fox's 1830 measurements in a Cornish mine (Fox 1830). SP was one of the several electrical methods studied by the Schlumberger brothers in the early 1900s (Schlumberger 1920; Allaud & Martin 1977), who inferred a relationship between Earth potentials and groundwater flow. Negative SP anomalies are associated with metalliferous ore bodies and are thought to be caused by gradients in oxidation state across the water table (Sato & Mooney 1960), but the contemporary use of SP prospecting in mining geophysics is limited. Noise levels are fairly high, and other electrical methods such as

DC resistivity, induced polarization, controlled-source electromagnetic (CSEM) sounding and magnetotelluric sounding all produce generally more useful results given the costs of getting people and equipment into the field. Importantly, quantitative interpretation of SP data is difficult, since temperature, permeability, porosity, conductivity, porewater chemistry and pressure all contribute to SPs. Today, SP studies are largely carried out as part of geothermal and volcanic studies (e.g. Corwin & Hoover 1979; Zlotnicki *et al.* 1998) since both hydrothermally driven groundwater flow and, to a lesser extent, thermal gradients generate electric potentials.

As with most electrical and electromagnetic methods, SP measurements can be made in the marine environment (Corwin 1976). Heinson *et al.* (1999) observed SP anomalies thought to be associated with an offshore extension of a graphite body. In what is

probably the first application of marine SP to the study of seafloor massive sulfide (SMS) deposits, Von Herzen *et al.* (1996) floated an electrode above the submersible Alvin and recorded negative potentials above the TAG hydrothermal mound. Cherkashev *et al.* (2013) report that deep-towed SP surveys have been used for the initial discovery of several SMS deposits associated with hydrothermal venting near mid-ocean ridges. Kawada & Kasaya (2017) observed negative SP anomalies over the Izena geothermal field, also using a deep-towed array. Sudarikov & Roumiantsev (2000) deep-towed an instrument package over a vent field on the Mid-Atlantic Ridge, and observed coincident negative SPs and negative redox potentials over a high-temperature black smoker vent. Safipour *et al.* (2017) made marine SP measurements over a known SMS deposit in the Tyrrhenian Sea, notable for not being associated with a currently active hydrothermal system, using a vertically lowered active-source EM system as the platform. While all the above studies observed negative SP anomalies, Beltenev *et al.* (2009) observed both negative and positive potentials, and not all their SMS target sites had anomalies, including the only actively venting site.

Most of the previous marine SP studies have used cables terminated with electrodes as the sensor, which is easy to do in the marine environment and allows signals to be integrated along the length of the antenna. However, towed arrays do have various limitations. Surface-towed arrays are subject to noise from wave motion, and are restricted to relatively shallow waters. Heinson *et al.* (1999) deep-towed a SP array, although water depths were only 100–300 m in their coastal study area. Arrays can be towed in deeper water (e.g. Cherkashev *et al.* 2013), but motion of cabled arrays in Earth's magnetic field is still a significant source of noise, which motivated Constable *et al.* (2016) to develop deep-towed electric field receivers with short (of order 1 m), rigid antennae for the purpose of CSEM sounding. However, deep-water towing fully occupies the vessel carrying out the survey, limits tow speeds to 1–2 kn (0.5–1 m s<sup>-1</sup>), and swell-induced ship motion is still transmitted through even long tow cables. It is also likely that if the tow cable is conductive it will generate noise through the Lorentz force by moving in Earth's magnetic field, as observed by Safipour *et al.* (2017).

An alternative is to mount electric field receivers on an autonomous underwater vehicle (AUV; sometimes called an unmanned underwater vehicle, UUV, although a UUV need not necessarily be autonomous). In a 2016 pilot study to test the idea of using AUV receivers as part of a marine CSEM survey, we equipped an AUV with DC-coupled electric field sensors to study marine SPs in an area where seafloor massive sulfides are thought to occur. The project was a cooperation between Fukada Salvage and Marine Works, which supplied the vessel and AUV, Ocean Floor Geophysics, which incorporated the sensors into the AUV package and supervised the dive logistics and Scripps Institution of Oceanography, which supplied the electric field sensors and participated in the data collection. This was not the first use of an AUV in measurements of SP: Sato *et al.* (2017) report that measurements were made in 2015 over an SMS deposit using the AUV 'Urashima' operated by JAMSTEC.

## 2 INSTRUMENTATION

The electric field sensor and recording system consisted of the pressure case and electronics package of the Vulcan instrument described by Constable *et al.* (2016), installed into the wet hull of an International Submarine Engineering Limited explorer-class AUV with a 3000 m depth capability. Silver–silver chloride electrodes

were mounted to the hard lifting points of the AUV using square section fiberglass tubing (Fig. 1). The use of the lifting points was an expediency to keep costs low and avoid compromising the integrity and hydrodynamics of the AUV body, although the rear electrodes, near the propulsion system, were significantly noisier than the forward electrodes. In future tests a more elaborate electrode mounting system would move the electrodes forward, and lower them so that they were in the water while the AUV was on the surface. Crossline electric fields were recorded across the forward electrode pair (1.865 m dipole length), inline electric fields were recorded between the forward and rear electrodes (two dipoles with a separation of 1.520 m), and vertical fields were recorded across a vertical pair of electrodes separated by 0.905 m, although the placement of the lower electrode meant that the vertical sensor was at an angle of 70.5° to the AUV body.

While the primary objective of the pilot study was CSEM operations using battery-powered, deployed CSEM transmitters, the CSEM amplifiers were modified to additionally record DC-coupled electric fields. The transformer-coupled chopper amplifier used in this project is described by Webb *et al.* (1985) and Constable (2013). Potential differences from the electrodes are chopped at 2 kHz using an FET bridge, coupled to the amplifier using a transformer with a modest step-up turns ratio, amplified, demodulated to remove the chopping frequency, low-cut filtered and passed to the analogue to digital converter (ADC) through another amplifier stage. For the DC channels, the demodulated signal was removed before the low-cut filter and passed to the ADC through a unity gain buffer amplifier. Total gain is about 1000 and amplifier noise below 1 Hz is about  $1 \times 10^{-7}$  V Hz<sup>-1/2</sup> and white.

Because the primary interest was CSEM collection, we measured electric fields across orthogonal pairs of electrodes, rather than measuring potential differences with respect to a common electrode, as is sometimes done for SP surveys (e.g. Sato *et al.* 2017). With reference to Fig. 1 we measured electric field crossline to the AUV using E2–E1 (positive to the right), inline to the AUV using both E2–E4 (positive to the front), E3–E1 (positive to the rear) and vertical using E5–E6 (positive down). Thus, all measurements were in the AUV frame of reference and were analysed as such, although for plotting, fields were reversed when the AUV reversed its heading.

The installation of the electric field sensors did not impact the AUV's other data streams and functions, which included multi-beam bathymetry, side-scan sonar, magnetic field, water chemistry, conductivity, temperature and depth. The navigation system is composed of inertial navigation, ultrashort base line (USBL) acoustics, depth sensors and bottom tracking. For the data presented below, our estimate is that horizontal position is accurate to better than 3 m, although with further processing it could be made accurate to about 1 m.

## 3 DATA COLLECTION

The study area was near the Iheya Minor Ridge in the Iheya prospect of the Okinawa Trough (Fig. 2), a backarc basin undergoing active rifting (e.g. Ren *et al.* 2002). The location was chosen because it is in an area of active hydrothermal circulation and known massive sulfide bodies (e.g. Yeats *et al.* 2017). Water depth was about 1500 m. Komori *et al.* (2017) collected drill cores extending about 100 m below seafloor in this area, and describe the geology as unaltered basalt underlain by hydrothermal sands, clays and gravels. Electrical resistivity of the cores was 0.4–40 Ωm, driven largely

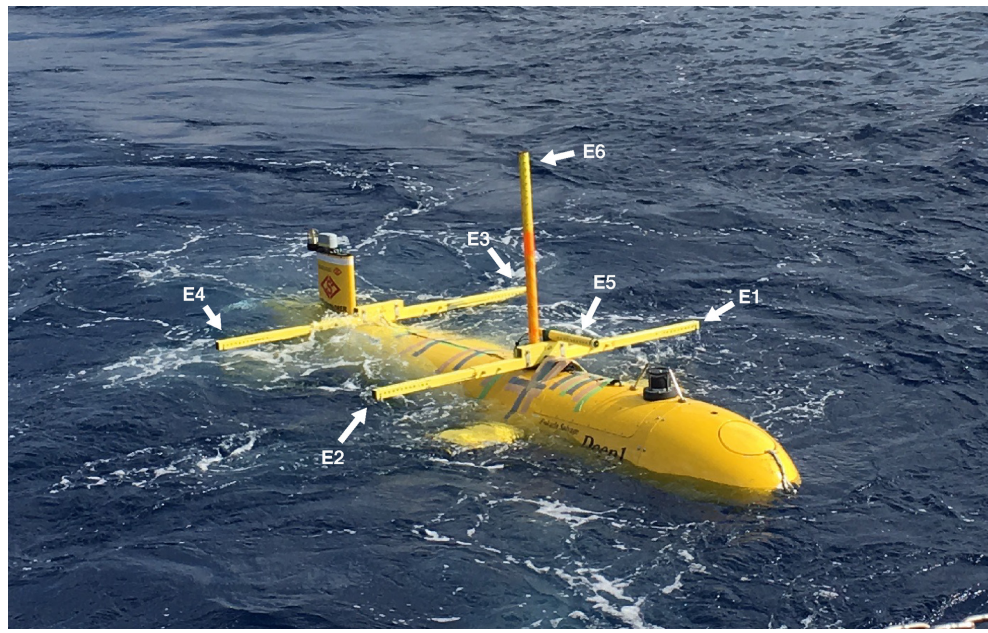


**Figure 1.** AUV on the surface after launch, showing electrode mounting system and positions of the electrodes (E1–E6).

by porosity and independent of clay or sulfide content, with the exception of one massive sulfide sample.

Data were collected during one 9.5 hr dive of the AUV. After a maneuver to calibrate the onboard magnetometers and the internal navigation systems, 20 lines each approximately 1 km long were run across the prospect, taking 7 hr. The AUV target altitude was 70 m and the vehicle speed was  $1.1 \text{ m s}^{-1}$ , limited by the drag of the electric field dipoles. The plan was to survey three lines spaced about 100 m apart in each of two orthogonal directions, repeating the pattern until the end of the dive to determine repeatability of the data. However, on the third pass the inertial navigation slipped by about 100 m, which offset lines 13, 14 and 15 and required resurveying one line (line 19) and thus provided a slightly richer data set. Eight channels of AC and DC electric field data were sampled at 250 Hz, synchronized to GPS time before and after deployment.

#### 4 DATA PROCESSING

Data processing consisted simply of averaging 30 s windows of electric field data, dividing by dipole length, and merging with AUV navigation. Standard errors in the mean were computed for the averages, which varied between 0.1 and  $5 \mu\text{V m}^{-1}$ . However, these error estimates are highly structured and clearly represent spatial variations in the electric field over the 30 s averages, during which time the AUV travelled 33 m. Signal on the DC channels at low frequencies had a red spectrum from about  $5 \times 10^{-7} \text{ V Hz}^{-1/2}$  at 1 Hz to about  $3 \times 10^{-4} \text{ V Hz}^{-1/2}$  at 0.01 Hz, representing some combination of sensor noise, variations in electric field during the 15 min of time-series for which the spectrum was computed and magnetotelluric noise.

The two inline electric field channels were averaged. By happenstance, much of the AUV induced noise on these two channels was of opposite sign. In particular, a strong peak in noise at 10.4 Hz due to the propulsion system was out of phase for these two channels and cancelled to some extent. A linear drift amounting to about  $0.1 \text{ mV m}^{-1}$  over the 7 hr data collection time was removed from

the data. After drift removal, there are still tares of up to  $0.1 \text{ mV m}^{-1}$  between line crossings and the two horizontal channels, which were levelled by manual adjustment. Fig. 3 shows the electric field averages after levelling.

It is worth considering the effect of motion (of velocity  $\mathbf{v}$ ) in Earth's magnetic field,  $\mathbf{B}$  as a source of noise, through the Lorentz force,  $\mathbf{E} = \mathbf{v} \times \mathbf{B}$ . The vertical field at Iheya is about  $30 \mu\text{T}$ , so the induced electric fields given the AUV velocity would be of order  $30 \mu\text{V m}^{-1}$ . This is above the estimated noise floor, but for the horizontal field it would not occur on the inline channels, and would be a constant for constant speed on the crossline channel, regardless of direction. The north component of the field is around  $34 \mu\text{T}$ , and so there might be a heading-dependent signal in the vertical measurement from the east–west component of motion, but for our survey pattern this component would be similar for all lines flown since the angle between the AUV and north was always about  $45^\circ$ . Fig. 4 shows an example of the data plotted for lines 4, 10 and 16 (the northerly SE–NW lines). Line to line reproducibility is good, and the mismatch is largely from residual levelling errors. Ignoring levelling offsets, the data are reproducible to better than  $5 \mu\text{V m}^{-1}$ .

#### 5 MODELLING SELF-POTENTIAL

The raw measurements are, necessarily, electric fields, which we need to integrate to recover true SPs. This is a straightforward exercise made complicated by the fact that the data are unevenly spaced, overlapping in places, and contain errors. We will appeal to regularized inversion, and specifically the Occam algorithm of Constable *et al.* (1987), to convert the unevenly spaced, noisy, electric field measurements into smoothly varying potentials on a uniform grid. This is a useful exercise for a number of reasons. Many readers, especially from the mining community, are used to looking at SP maps, not electric field maps. Also, the magnitude of the SP anomaly can be recovered and two vector measurements can be reduced to a single scalar quantity.

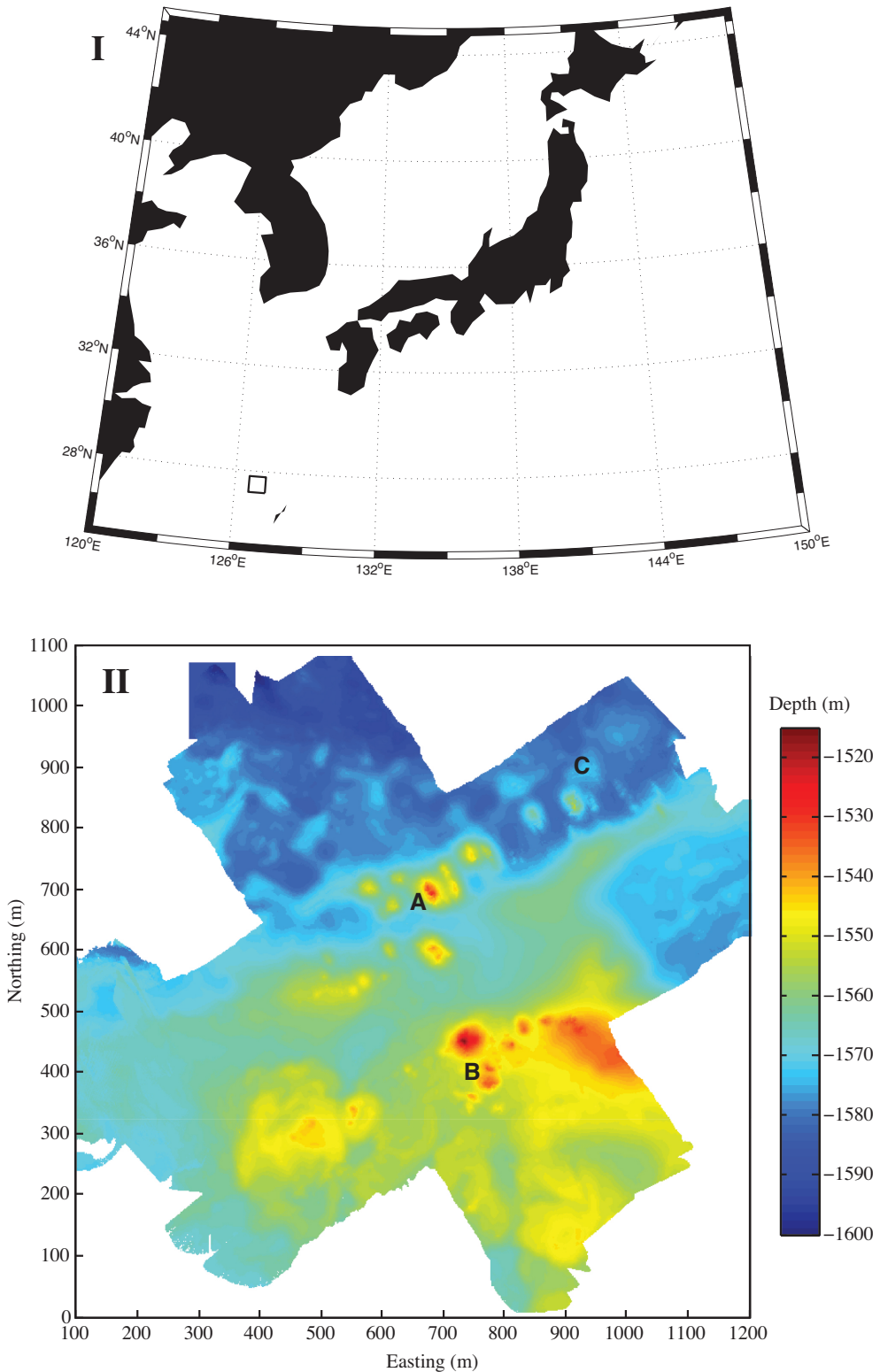


**Figure 2.** Location of the survey area (I), and bathymetry as recorded by the AUV's multibeam (II). The positions of the observed SP anomalies are shown by A, B and C.

### 5.1 Regularized mapping

The Occam inversion method introduced regularization to nonlinear inversion of geophysical data, but a key aspect of the algorithm is

the assignment of a target data misfit  $\chi_*^2$  and then the use of a line search over the Lagrange multiplier  $\mu$  at each iteration in order to achieve the target misfit. Unlike the original nonlinear applications, for the present study the integration of electric fields to recover SP

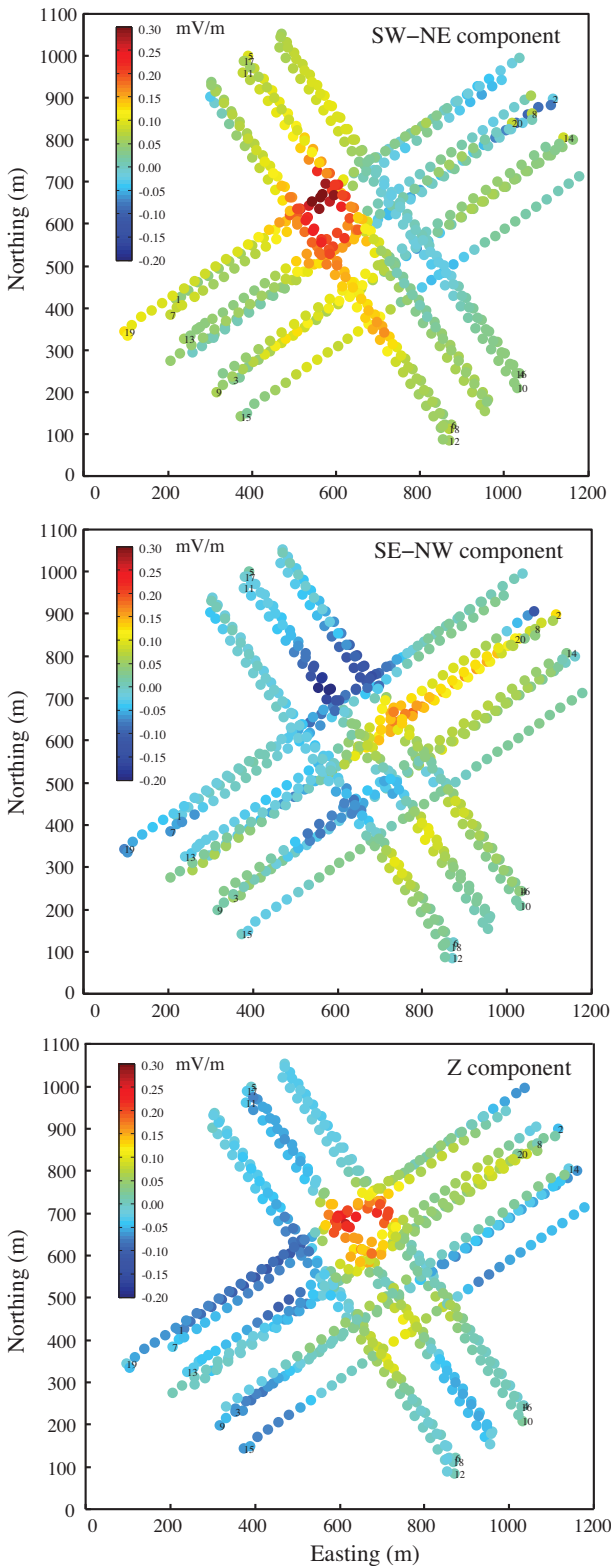


**Figure 3.** Electric field data, 30 s averages after levelling. The line numbers indicate the start of the line. The positive directions are NE, NW and down, respectively.

is a linear forward problem, which can always be cast as

$$\hat{\mathbf{d}} = \mathbf{G}\mathbf{m}, \quad (1)$$

where  $\hat{\mathbf{d}}$  are the predicted data values,  $\mathbf{G}$  a matrix of weights describing the linear forward problem and  $\mathbf{m}$  is a vector of model parameters. Note that although  $\mathbf{m}$  is always a column vector, it can represent a 2-D surface by taking sequential columns from a 2-D matrix and stacking them together. Given an appropriate choice of  $\mu$ , the regularized model is given by

$$\mathbf{m} = [\mu \mathbf{R}^T \mathbf{R} + (\mathbf{WG})^T \mathbf{WG}]^{-1} (\mathbf{WG})^T \mathbf{Wd}, \quad (2)$$

where  $\mathbf{R}$  is a matrix generating some penalty on the model, usually a roughness measure obtained by taking first differences of adjacent parameters,  $\mathbf{W}$  is a diagonal matrix of reciprocal data errors and  $\mathbf{d}$  of course contains the observed data.

The Lagrange multiplier,  $\mu$ , trades off roughness against data misfit. One might expect that for linear problems, misfit can be driven to zero as long as there are more model parameters than data. However, if there are multiple, inconsistent data at a given location, or at least close enough that they are influenced by a single model parameter, this may not be the case. Then, no matter how rough one allows the model to become (small  $\mu$ ) there will be some minimum misfit associated with incompatible data.

Before we use this method to recover SP, we can demonstrate its use by converting the vertical electric field data shown in Fig. 3 into a smooth map of vertical electric field on a uniform grid. The vertical component, which cannot easily be measured on land, shows clearly where the potential field anomalies are localized. The problem of making a map of uniformly spaced nodes from unevenly spaced, noisy, overlapping data is simply a linear inverse problem where the forward model  $\mathbf{G}$  is just the value of the data themselves, the data  $\mathbf{d}$  are the unevenly spaced vertical electric field measurements and the model  $\mathbf{m}$  are interpreted vertical electric fields on a uniform grid which extend beyond the area of measurement. In practice, the forward problem could be an average of the nearest four nodes to a given data point, weighted by distance. Fig. 5 shows a smooth map of the vertical electric field data shown in Fig. 3. The averaging errors have been used and the data can be fit to root-mean-square (RMS) misfit of 0.02, but the map has been smoothed to an RMS misfit of 50. Three areas of elevated electric field are evident in the smoothed model of the data. The model grid extends to the edges of the rectangular plotting area, but with a first derivative roughness penalty, the map will go flat where there are no data constraints. While some extrapolation beyond the data is reasonable for a smoothed model, and data acquired along lines will be sensitive to off-line anomalies (e.g. Kawada & Kasaya 2017), we have only plotted the model within 100 m of the data locations.

## 5.2 Regularized self-potential estimates

For mapping SP, rather than fields, we appeal to the relationships between electric field and potential:  $E_x = -dV/dx$  and  $E_y = -dV/dy$ . However, it is at this point we have to acknowledge that what we measure is not electric field, but potential difference

$$V_2 - V_1 = - \int_{x_1}^{x_2} \mathbf{E} \cdot d\mathbf{x} \quad (3)$$

(Scott 1966, eqs 1.7–2) which, when normalized by electrode spacing  $\Delta x$  on a straight antenna, becomes

$$\frac{V_2 - V_1}{\Delta x} \approx -E_x = \frac{dV}{dx}. \quad (4)$$

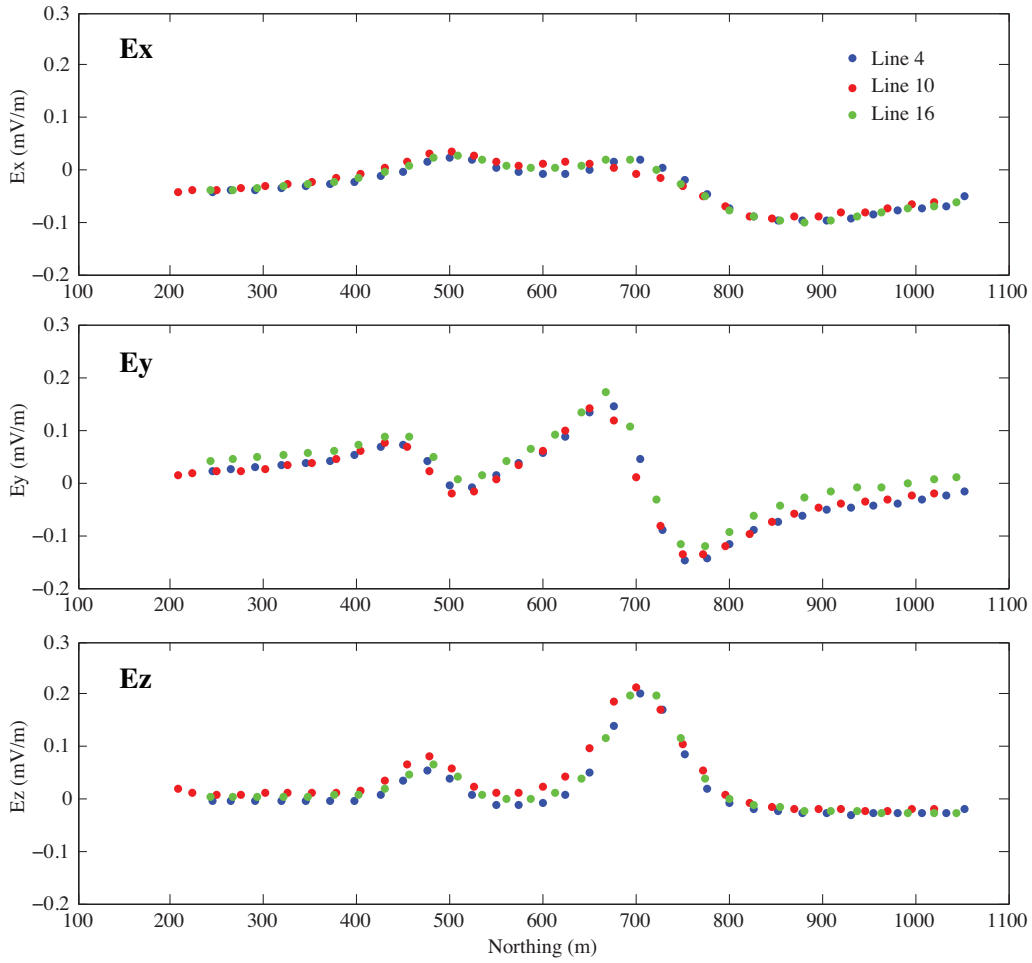


**Figure 4.** Electric field data, 30 s averages after levelling, for line numbers 4, 10 and 16.

Note the change in sign. It appears to be normal practice, as has been done in this paper, to use potential difference and electric field interchangeably, but in order to get the sign of the SP anomaly correct we have to account for the difference in sign between the two.

With reference to Fig. 6 we have two approximations to each of  $dV/dx$  and  $dV/dy$ , one from each edge of the box containing the data point at  $(x, y)$  with potentials  $V_1, V_2, V_3$  and  $V_4$  at the corners:

$$\frac{dV}{dx} \approx \frac{V_2 - V_1}{dx} \quad \text{and} \quad \frac{dV}{dx} \approx \frac{V_4 - V_3}{dx}, \quad (5)$$

and

$$\frac{dV}{dy} \approx \frac{V_3 - V_1}{dy} \quad \text{and} \quad \frac{dV}{dy} \approx \frac{V_4 - V_2}{dy}. \quad (6)$$

Again, we can use a weighted average of these using  $x_f$  and  $y_f$ , the offset of the data point to the lower left model node, to form the forward problem. We need the constant of integration, obtained by setting the potential of the lower left node to zero as an additional data point. In this case the data  $\mathbf{d}$  are now the unevenly spaced horizontal electric fields rotated from the AUV frame of reference into the  $x$  and  $y$  directions (east and north), the model  $\mathbf{m}$  is potential on a regular grid and the  $\mathbf{G}$  matrix extracts potential differences to predict electric fields. Note that by casting the recovery of the SP as an inverse problem, we have not had to integrate the observed electric fields (which for noisy, unevenly spaced data is difficult),

but have only had to difference evenly spaced potentials as part of the forward problem.

Fig. 7 shows a reconstruction of the SP derived from the horizontal electric field data in this way, fitting the electric field data to RMS 1.0 with a  $5 \mu\text{V m}^{-1}$  noise floor. The largest anomaly (A) is a little more than 25 mV, positioned slightly north of the centre of the survey area, with a smaller 15 mV anomaly (B) positioned to the south over the area of highest bathymetric relief. The SP low extends along the ridge structure to the north-east of the survey area (C). Also shown in the figure are the directions of the horizontal potential differences, scaled by amplitude. These, of course, are the data that went into creating the potential anomaly plot, but the fact that they point along the potential gradients validates the integration process described above. They also highlight the fact that the electric fields go to zero at the extremes in the potential, and show that the data are spatially smooth and generally agree between repeat lines. Again, we have extended the model 100 m beyond the region covered by data, and the reader should be aware that between the lines of data and in the extrapolated region the regularization smoothing plays a role in determining the model.

### 5.3 Modelling current dipoles

The full width at half-maximum for anomalies (A) and (B) is of order 100 m or less, compared with an AUV flying height of 70 m, which implies that the potential field sources are likely localized and

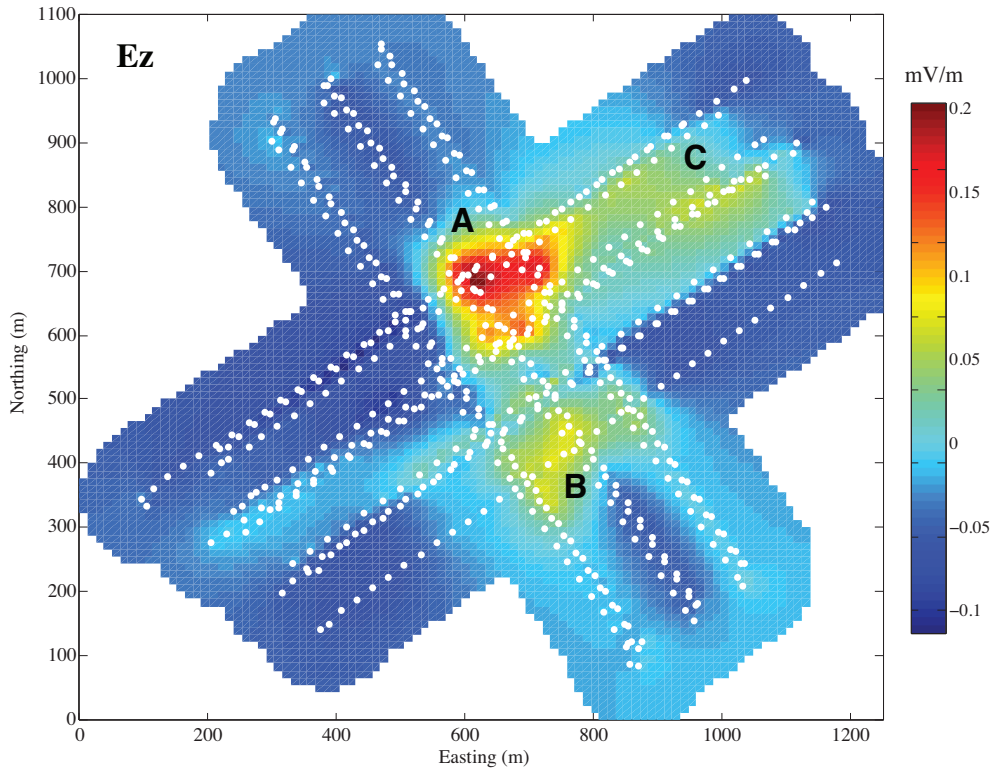


**Figure 5.** Smooth map of the vertical electric field data shown in Fig. 3. White dots show the position of the actual data. The map is only plotted within a distance of 100 m from the data locations. Anomalies (A), (B) and (C) are referenced in the text.

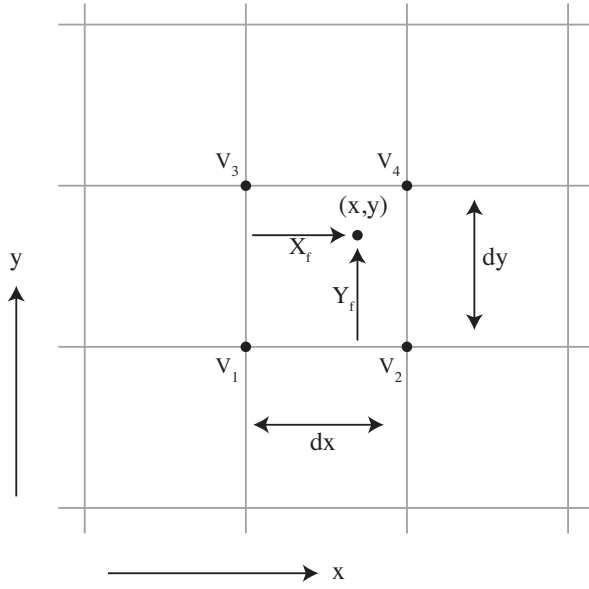


**Figure 6.** Mesh structure for estimating self-potential from electric fields.

quite close to the seafloor. We can test this by modelling the observed electric field data as collected by the AUV using discrete dipole current sources, parametrized by their  $(x, y, z)$  coordinates, dipole length and total current. Sparsely parametrized models are amenable to inversion using the Marquardt (1963) method, which was used here. We could invert for three dipoles, amounting to 15 parameters (position, current and separation for each dipole). Adding additional dipoles destabilizes the inversion. The starting model had a vertical dipole positioned approximately under each of anomalies (A), (B)

and (C). Data were inverted as collected in the AUV coordinate system (inline, crossline and vertical electric fields) by taking into account AUV heading for each data point. Averaging errors were used, but with a noise floor of  $10 \mu\text{V m}^{-1}$ . An understanding of the host conductivity is required to carry out the modelling. In this case, the conductivity of the sea water between the AUV sensors and the seafloor is almost constant and well measured by the AUV. The seafloor conductivity is less well known, although we have some estimates as discussed below, but Kawada & Kasaya (2017) noted that seafloor conductivity was not a big factor in localizing dipole source locations. The response of the inverted model fit the data to RMS of 3.8, and generally reproduces the features seen in the data set (Fig. 8). The combined fit to the three components of the field is reassuring from a data validation perspective.

The modelled negative pole under anomaly (A) is at a depth of 1577 with a current strength of  $-48.5 \text{ A}$ , the negative pole under anomaly (B) is at a depth of 1587 m with a current strength of  $-41.3 \text{ A}$ . Both of these poles are essentially at the seafloor. The negative pole under anomaly (C) is at a depth of 2125 m and positioned at a northing of 1224 m. The greater depth and position outside the data collection area are clearly an attempt to fit the broader anomaly in this part of the data, which is not well fit using a single dipole. In all cases, the positive return poles, included to enforce charge balance, have to be at depths greater than 1000 m below the seafloor in order to fit the data (and can be placed essentially at infinity). From this we infer that the return current path for the sources positioned near the seafloor is probably diffuse and located at considerable depth.

The purpose of this modelling is simply to demonstrate that the sources of the SP anomalies are localized and close to the seafloor. More sophisticated approaches to the inversion of SP data certainly

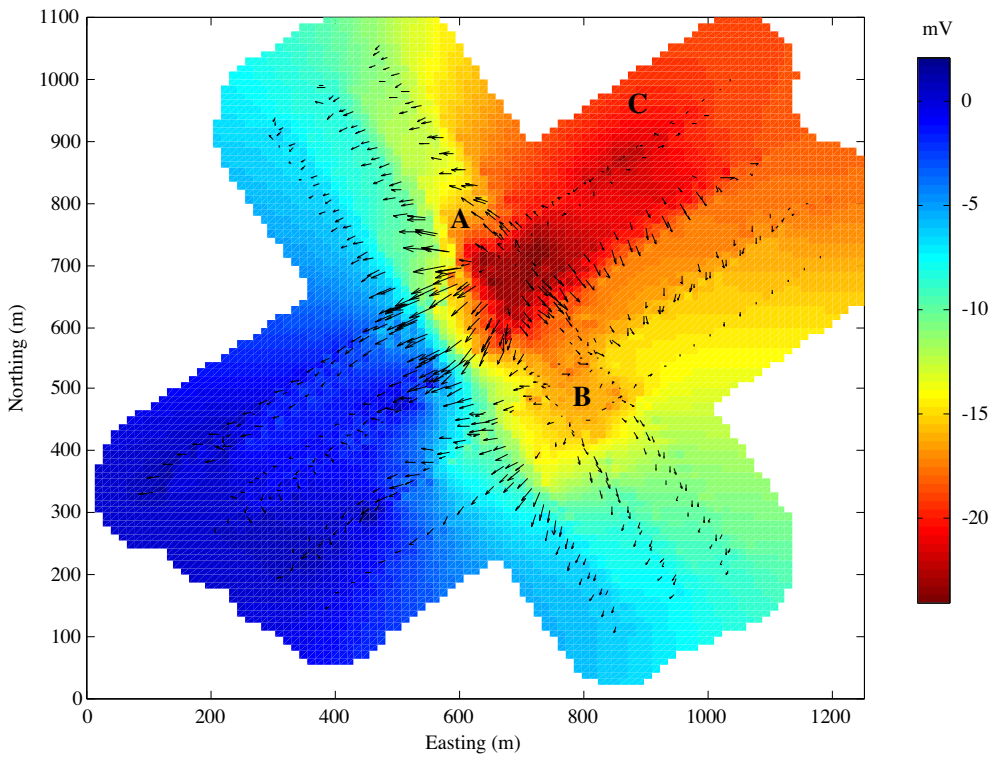


**Figure 7.** Self-potential derived from  $E_x$  and  $E_y$  data shown in Fig. 4 by regularized integration as described in the text. Arrows show the directions of the potential differences as measured by the AUV, scaled by amplitude.

exist (e.g. Jardani *et al.* 2008), but are beyond the scope of the current paper.

## 6 INTERPRETATION

On land, SP anomalies are caused by mineralization, thermal gradients or streaming potentials (or some combination of these). Streaming potentials are expected to be trivially small in the conductive marine environment, and marine SP anomalies are generally attributed either to hydrothermal circulation or to the Sato & Mooney (1960) ‘geo-battery’ effect caused by conductive mineral deposits linking regions of differing oxidation potential (Kawada & Kasaya 2017).

SP anomalies predicted by the Sato & Mooney (1960) electrochemical model of mineralized bodies are negative, and on land this is supported by the majority of observations. This model assumes that oxidation potential is higher near the surface, and one would expect a similar oxidation gradient near the seafloor. Corwin (1976) notes that measurements in marine sediments show lower oxidation potentials, and reports negative SP anomalies measured in shallow coastal water ( $\approx 10$  m) near land ore deposits with associated SP anomalies. SP anomalies generated by the geo-battery mechanism are expected to be dipolar in nature, and both Safipour *et al.* (2017) and Kawada & Kasaya (2017) observed near-seafloor dipolar anomalies and interpreted them as caused by the Sato & Mooney (1960) mechanism over SMS deposits.

Hydrothermal fluids emanating from seafloor vents are highly reducing compared to sea water, also leading to negative SP anomalies. Kawasumi & Chiba (2017) calculated the oxygen fugacity of hydrothermal fluids in the Iheya area to be about  $10^{-28}$  Pa, which is much less than in sea water. Yamamoto *et al.* (2017) measured a potential more than 600 mV lower than distal sea water in venting

hydrothermal fluids at the Iheya North Aki field. Yamamoto *et al.* (2017) measured negative potentials using probes in contact with hydrothermal fluids. Sudarikov & Roumiantsev (2000) observed coincident negative SPs and highly localized negative redox potentials about 5–35 m above a high-temperature vent at the Mid-Atlantic Ridge.

Although we cannot distinguish between a geo-battery mechanism and a hydrothermal venting source based on the polarity of the SP anomaly, the localized, near-seafloor source of the SP anomalies, as modelled for anomalies (A) and (B), is consistent with hydrothermal venting as the causative mechanism. If the source of the SP anomalies was SMS mineralization, one might expect to see a less localized and more dipolar SP signal. Oxidation–reduction potential (ORP) measurements made by the AUV suggest that hydrothermal venting is occurring in the study area, although at a flight height of 70 m these measurements cannot localize the sources. We should note that there is no evidence that the ORP signals have affected our electric field measurements. Anomalies (A) and (B) are located on or near the two most prominent seafloor mounds in the area, as recorded by the AUV bathymetry and side-scan data (Fig. 2), although the larger anomaly (A) is located over the smaller mound, which is about 20 m wide, compared with 50 m wide for (B). The height of the mounds is comparable to their width. The more diffuse SP anomaly to the north–east (C), may be associated with smaller mounds and a ridge in that area. The association of the SP anomalies with the mounds lends further support to the idea that hydrothermal venting is the cause.

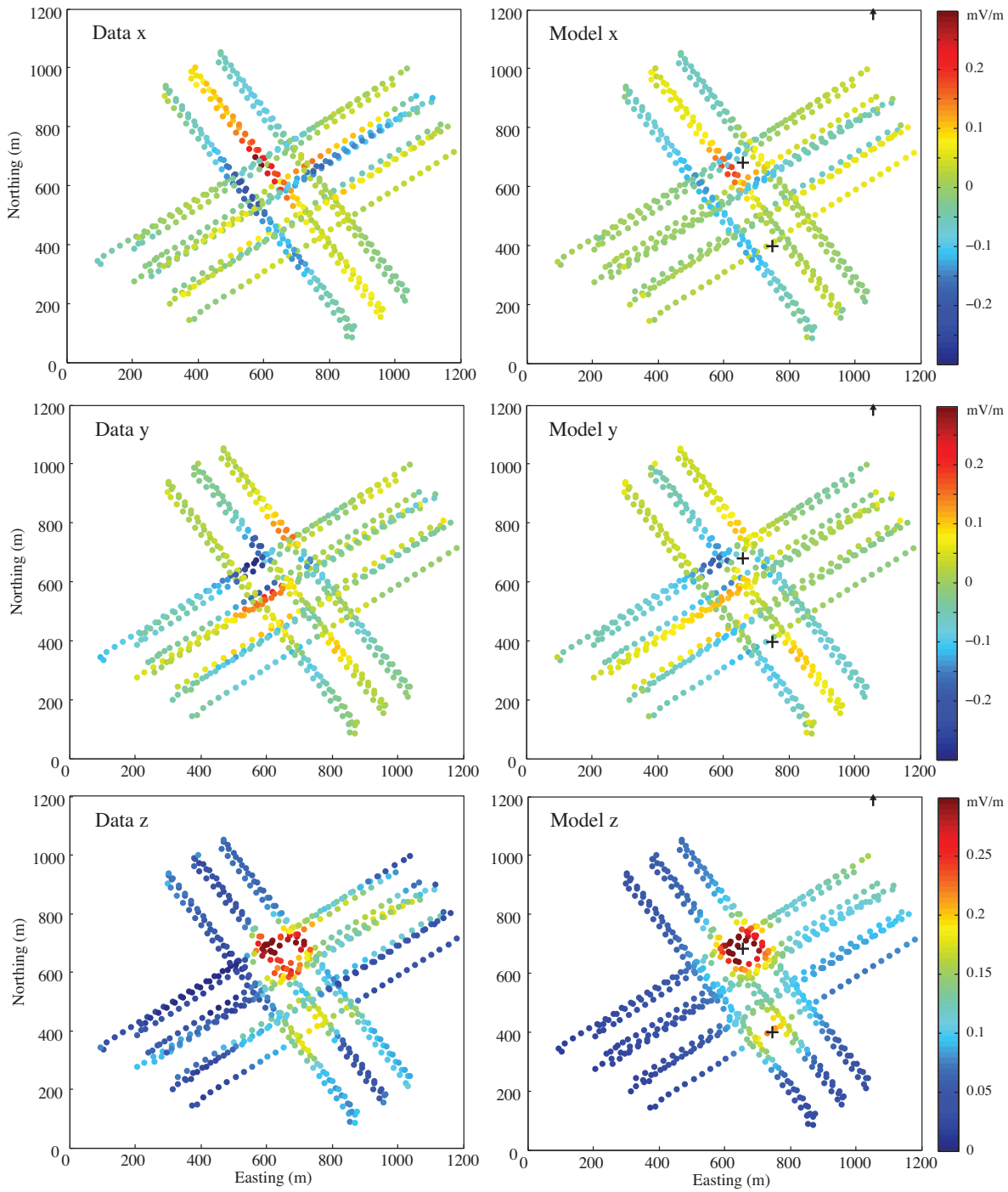


**Figure 8.** Electric field data as collected (left panels), and the predicted response of a model consisting of three negative current poles (right panels—pole positions shown as plus signs and, for pole C, an arrow indicating a position just outside the plotting region). Here  $y$  is inline electric field,  $x$  is crossline electric field and  $z$  is vertical electric field. Note that the sign of the horizontal electric field can reverse if the AUV reverses direction.

## 7 SEAFLOOR APPARENT CONDUCTIVITY

Determining whether the causative mechanism of the SP anomalies is hydrothermal venting or SMS mineralization is made complicated by the fact that venting and mineralization are often associated. Indeed, Cherkashev *et al.* (2013) used the SP anomalies caused by venting to explore for SMS deposits, and both venting and mineralization are known to occur in the Iheya area (Yeats *et al.*

2017). If the observed AUV SP anomalies are associated with SMS mineralization, one would also expect them to be associated with high electrical conductivities (Cairns *et al.* 1996). Spagnoli *et al.* (2016) measured the electrical conductivity of about 20 SMS samples and observed electrical conductivities greater than  $1 \text{ S m}^{-1}$  and as high as  $100 \text{ S m}^{-1}$ . Host basalts had conductivities in the range of  $0.01\text{--}0.05 \text{ S m}^{-1}$ . Mineralized breccias, common in hydrothermal systems, had conductivities  $0.15\text{--}0.5 \text{ S m}^{-1}$ . As noted in Section 1,

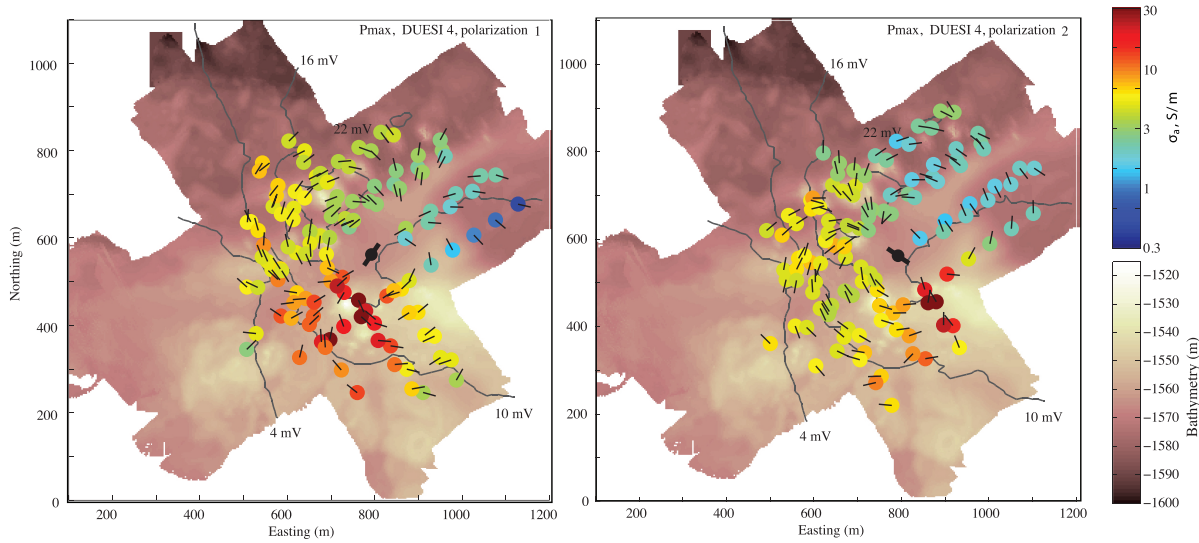


**Figure 9.** Apparent conductivity  $\sigma_a$  (coloured disks –  $\log_{10}$  scale) overlain on bathymetry for two polarizations of CSEM transmission from a deployed transmitter (centred black symbol). Transmission frequency is 14 Hz, and the black lines show the directions of the polarization ellipse maxima recorded by the AUV. SP anomaly contours from Fig. 7 are shown as dark grey lines.

marine CSEM measurements were made as part of this study, accomplished by deploying a battery powered CSEM electric field transmitter near the centre of the survey area (Deployed Undersea Electromagnetic Source Instrument). The transmitter broadcast 20 A at a frequency of 2 Hz and harmonics across an orthogonal pair of 10 m transmission antennae, alternating between polarities every 30 s. CSEM fields were recorded out to ranges of about 400 m by the AC-coupled electric field channels of the AUV receiver system. Transmitter and AUV locations were obtained using USBL acoustic navigation from the vessel, supplemented in the case of the AUV by doppler velocity logs. We estimate position errors are of order 3 m. Electric fields were converted to apparent conductivity  $\sigma_a$  by modelling the horizontal polarization ellipse maxima with a seafloor half-space for the particular source–receiver geometry of every data point, using a six-layer water conductivity profile obtained by the AUV sensors. Apparent conductivities for the 14 Hz harmonic, along with polarization ellipse directions, are shown in Fig. 9. We have neglected data at source–receiver ranges of less than 100 m to avoid navigation errors larger than about 5 per cent propagating into apparent conductivity. Not every AUV position recorded both polarizations above the noise floor.

Apparent conductivities vary between about 0.5 and 30  $S\ m^{-1}$ . The two transmitter polarizations produce generally compatible results, the differences being well within what is expected from the different sensitivities of the two polarizations and the effects of non-homogeneous structure. For example, the area of high conductivity south of the transmitter seems to follow the inline component, which has a larger vertical CSEM electric field.

To the northeast of the transmitter, apparent conductivities are about 1–2  $S\ m^{-1}$ , consistent with marine sediments or fractured, near-surface extrusive volcanics (Komori *et al.* 2017). Sub-bottom acoustic profiling by the AUV confirms that there are sediments in this area but not others. Apart from the northeast, most of the survey area has apparent conductivities that are higher than would be expected for normal seafloor, around 5  $S\ m^{-1}$  to the west and reaching 30  $S\ m^{-1}$  south of the transmitter. These apparent conductivities are entirely consistent with those observed by Cairns *et al.* (1996) around the TAG hydrothermal mound. One needs to be cautious interpreting apparent conductivities, as they have no

depth sensitivity and cannot localize structure. For example, here we have plotted apparent conductivities at the locations of the AUV receiver, on the grounds that sensitivity to seafloor conductivity is a maximum beneath the transmitter and receiver (see e.g. fig. 11 of Constable 2010), and the transmitter is fixed. However, if the transmitter is situated on conductive material, all apparent resistivities will reflect this, and the signals are also sensitive to conductivities between transmitter and receiver. However, apparent conductivities are a fairly reliable indicator of the lateral extent of variations in the data, and high apparent conductivities are an indication of rocks at least this conductive somewhere in the section, although the signature could be smeared.

We observe the highest conductivities, up to 30  $S\ m^{-1}$ , over the smaller SP anomaly (B), although the larger SP anomaly at (A) is still associated with apparent conductivities above about 3  $S\ m^{-1}$ . Just as the SP signals could be generated by hydrothermal venting or SMS deposits, elevated conductivities can be generated by elevated temperature or mineralization. Komori *et al.* (2017) observed conductivities between 0.03 and 3  $S\ m^{-1}$  for samples of basalts, sands, clays and gravels collected from boreholes in this area and measured at room temperature in the laboratory. However, they noted that logging while drilling recorded conductivities up to an order of magnitude greater than the room temperature measurements and attributed this to increased seafloor temperatures. They observed a correlation of conductivity with porosity, but not with clay content or sulfide content, but the sulfide contents were all 25 per cent or less (it is known that disseminated sulfides do not necessarily increase conductivity). The conductive smectite clay caps commonly found associated with land geothermal systems are not characteristic of marine hydrothermal systems because the geological setting is very different (e.g. Humphris *et al.* 1995).

Given these observations, it is likely that the high conductivities and high SP anomalies are not caused by a single, common mechanism. Conductivities of 30  $S\ m^{-1}$  are higher than can be obtained by sea water at any temperature (Quist & Marshall 1968), and the half-space model used for apparent conductivity will underestimate peak conductivity, so high apparent conductivities at anomaly (B) are most easily interpreted as seafloor massive sulfides. While we cannot rule out that conductivities of 3–10  $S\ m^{-1}$  at anomaly (A) are

caused by lower concentrations of sulfides, these could be associated with elevated temperature.

Although apparent conductivity measurements suggest massive mineralization in at least part of the study area, the nature of the SP signals suggests a hydrothermal origin for the SP anomalies. Without further work we cannot definitively attribute the SP anomalies to mineralization, hydrothermal venting or both. However, since seafloor hydrothermal venting is intimately linked to mineralization, in either case SP measurements represent a useful tool for seafloor mineral exploration. The CSEM part of this study will be reported separately in more detail, which will include inversion of the data to localize conductivities with depth and lateral position.

## 8 CONCLUSIONS

We have developed a system to measure DC electric fields using an AUV. A pilot study over the Iheya prospect in the Okinawa Trough mapped three components of electric field over a 1 km × 1 km area with 7.5 hr data collection. Although the observed electric fields are small (of order a few hundreds of microvolts per metre), stacking errors, spectral estimates and repeat data all indicate that measurement errors are smaller,  $1\text{--}5 \mu\text{V m}^{-1}$ , making the AUV-mounted sensors a viable way of observing marine SP. The survey pattern was repeated three times, showing excellent repeatability between passes over similar transects. When integrated, the electric fields yielded negative SP anomalies of  $-15$  to  $-25$  mV, consistent with sources localized at the seafloor and associated with moderate to high apparent electrical conductivity, measured independently using a deployed CSEM transmitter. Although high conductivities suggest that the anomalies are associated with seafloor mineralization, the source mechanism are more likely due to hydrothermal venting. In either case, we have demonstrated that AUV-mounted electric field sensors are an accurate and efficient way to prospect for seafloor massive sulfides and hydrothermal activity.

For the initial tests presented here, the electrode mounting hardware was simple and made out of available materials, and the resulting drag limited the speed of the AUV. For future measurements, one could streamline the dipoles to reduce drag and restore the AUV's operational speed of 4 kn. Combined with an endurance of around 18 hr, this would allow over 100 line km of data to be collected in 1 d, while leaving the support ship to carry out other work between launch and recovery. Marine electrodes are subject to drift, especially on initial deployment, but the drift rate is too slow to compromise anomaly detection. Calibration maneuvers could be carried out periodically to remove offsets between the horizontal channels.

## ACKNOWLEDGEMENTS

First and foremost, the authors would like to thank Hideo Kimura, Fukada Salvage and Marine Works not only for providing the vessel and AUV time to make these measurements but also for taking the risk of mounting unnatural equipment to their AUV. We thank the captain and crew of the Shin Kai Maru and the engineers and technicians of the Scripps Marine EM Laboratory. The Scripps Seafloor Electromagnetic Methods Consortium and an anonymous donor funded the Scripps costs to carry out this study. Reviews of the initial manuscript by Tada-nori Goto and Andrei Revil led to significant improvements during revision. Data and code used in this paper can be obtained from <http://marineemlab.ucsd.edu/Projects/AUV>.

## REFERENCES

- Allaud, L. & Martin, M., 1977. *Schlumberger, The History of a Technique*, John Wiley.
- Beltenev, V. *et al.*, 2009. New data about hydrothermal field on the Mid-Atlantic Ridge between  $11^{\circ}\text{--}14^{\circ}\text{N}$ : cruise of the R/V Professor Logatchev, *InterRidge News*, **18**, 13–17.
- Cairns, G.W., Evans, R.L. & Edwards, R.N., 1996. A time domain electromagnetic survey of the TAG hydrothermal mound, *Geophys. Res. Lett.*, **23**, 3455–3458.
- Cherkashev, G.A. *et al.*, 2013. Massive sulfide ores of the northern equatorial Mid-Atlantic Ridge, *Oceanology*, **53**, 607–619.
- Constable, S., 2010. Ten years of marine CSEM for hydrocarbon exploration, *Geophysics*, **75**, 75A67–75A81.
- Constable, S., 2013. Review paper: instrumentation for marine magnetotelluric and controlled source electromagnetic sounding, *Geophys. Prospect.*, **61**, 505–532.
- Constable, S., Kannberg, P.K. & Weitemeyer, K., 2016. Vulcan: a deep towed CSEM receiver, *Geochem. Geophys. Geosyst.*, **17**, 1042–1064.
- Constable, S.C., Parker, R.L. & Constable, C.G., 1987. Occam's inversion: a practical algorithm for generating smooth models from EM sounding data, *Geophysics*, **52**, 289–300.
- Corwin, R., 1976. Offshore use of the self-potential method, *Geophys. Prospect.*, **24**, 79–90.
- Corwin, R.F. & Hoover, B.H., 1979. The self-potential method in geothermal exploration, *Geophysics*, **44**, 226–245.
- Fox, R.W., 1830. On the electro-magnetic properties of metalliferous veins in the mines of Cornwall, *Phil. Trans. R. Soc. Lond. A*, **120**, 399–414.
- Heinson, G., White, A., Constable, S. & Key, K., 1999. Marine self potential exploration, *Explor. Geophys.*, **30**, 1–4.
- Humphris, S.E. *et al.*, 1995. The internal structure of an active sea-floor massive sulfide deposit, *Nature*, **377**, 713–716.
- Jardani, A., Revil, A., Bolève, A. & Dupont, J.P., 2008. Three-dimensional inversion of self-potential data used to constrain the pattern of groundwater flow in geothermal fields, *J. geophys. Res.*, **113**, B09204, doi:10.1029/2007JB005302.
- Kawada, Y. & Kasaya, T., 2017. Marine self-potential survey for exploring seafloor hydrothermal ore deposits, *Sci. Rep.*, **7**, doi:10.1038/s41598-017-13920-0.
- Kawasumi, S. & Chiba, H., 2017. Redox state of seafloor hydrothermal fluids and its effect on sulphide mineralization, *Chem. Geol.*, **451**, 25–37.
- Komori, S. *et al.*, 2017. Depth profiles of resistivity and spectral IP for active modern submarine hydrothermal deposits: a case study from the Iheya North Knoll and the Iheya Minor Ridge in Okinawa Trough, Japan, *Earth Planets Space*, **69**, doi:10.1186/s40623-017-0691-6.
- Marquardt, D.W., 1963. An algorithm for least-squares estimation of non-linear parameters, *J. Soc. Ind. Appl. Math.*, **11**, 431–441.
- Quist, A.S. & Marshall, W.L., 1968. Electrical conductances of aqueous sodium chloride solutions from 0 to  $800^{\circ}$  and at pressure to 4000 bars, *J. Phys. Chem.*, **72**, 684–703.
- Ren, J.Y., Tamaki, K., Li, S.T. & Junxia, Z., 2002. Late Mesozoic and Cenozoic rifting and its dynamic setting in Eastern China and adjacent areas, *Tectonophysics*, **344**, 175–205.
- Safipour, R., Hötzl, S., Halbach, J., Jegen, M., Petersen, S. & Swidinsky, A., 2017. A self-potential investigation of submarine massive sulfides: Palinuro Seamount, Tyrrhenian Sea, *Geophysics*, **82**, A51–A56.
- Sato, M. & Mooney, H.M., 1960. The electrochemical mechanism of sulphide self-potentials, *Geophysics*, **3**, 226–249.
- Sato, S., Goto, T., Kasaya, T., Kawada, Y., Iwamoto, H. & Kitada, K., 2017. Noise reduction method of marine spontaneous electric field data using independent component analysis (in Japanese), *Butsuri-tansa (Geophys. Explor.)*, **70**, 42–55.
- Schlumberger, C., 1920. *Study of Underground Electrical Prospecting*, translated by S.F. Kelly, Paris. 99 pp.
- Scott, W.T., 1966. *The Physics of Electricity and Magnetism*, 2nd edn, Wiley.
- Spagnoli, G., Hannington, M., Bairlein, K., Hördt, A., Jegen, M., Petersen, S. & Laurila, T., 2016. Electrical properties of seafloor massive sulfides, *Geo-Mar. Lett.*, **36**, 235–245.

- Sudarikov, S.M. & Roumiantsev, A.B., 2000. Structure of hydrothermal plumes at the Logatchev vent field, 14°45'N, Mid-Atlantic Ridge: evidence from geochemical and geophysical data, *J. Volc. Geotherm. Res.*, **101**, 245–252.
- Von Herzen, R.P., Kirklin, J. & Becker, K., 1996. Geoelectrical measurements at the TAG hydrothermal mound, *Geophys. Res. Lett.*, **23**, 3451–3454.
- Webb, S.C., Constable, S.C., Cox, C.S. & Deaton, T.K., 1985. A sea-floor electric field instrument, *J. Geomagn. Geoelectr.*, **37**, 1115–1129.
- Yamamoto, M., Nakamura, R., Kasaya, T., Kumagai, H., Suzuki, K. & Takai, K., 2017. Spontaneous and widespread electricity generation in natural deep-sea hydrothermal fields, *Angew. Chem., Int. Ed.*, **56**, 5725–5728.
- Yeats, C.J. *et al.*, 2017. Actively forming Kuroko-type volcanic-hosted massive sulfide (VHMS) mineralization at Iheya North, Okinawa Trough, Japan, *Ore Geol. Rev.*, **84**, 20–41.
- Zlotnicki, J., Boudon, G., Viodé, J.P., Delarue, J.F., Mille, A. & Bruère, F., 1998. Hydrothermal circulation beneath Mount Pelée inferred by self potential surveying. Structural and tectonic implications, *J. Volc. Geotherm. Res.*, **84**, 73–91.